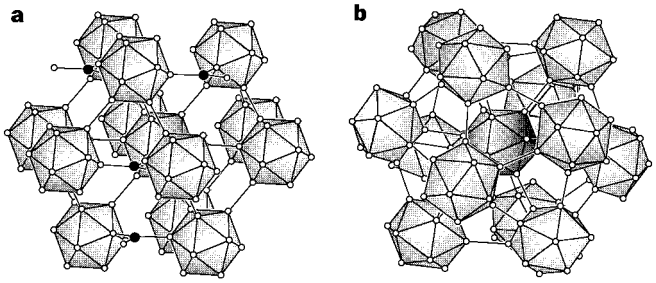

Figure 4 a, A part of the B_6O structure showing c.c.p. packing (slightly distorted) of B_{12} icosahedra with O atoms (filled circles) in the close-packed layers. Each O is bonded to a B in three separate icosahedra. The centres of the outer 12 icosahedra are at the vertices of a cuboctahedron. **b**, A fragment of the β-rhombohedral boron structure. The central B_{12} unit is surrounded by 12 other B_{12} icosahedra whose centres are at the vertices of an icosahedron. The whole assembly is an icosahedron of icosahedra ('super-icosahedron'). Such a super-icosahedron also occurs in YB_{66} (ref. 27).

structural units: a central B_{12} icosahedron is surrounded icosahedrally by 12 other B_{12} units forming a 'super-icosahedron' (Fig. 4b). In our icosahedral MTPs of B_6O, such a super-icosahedron may serve as the nucleus for the observed icosahedral packing of B_{12} units. Growth occurs by addition of successive layers of B_{12} icosahedra to each triangular face. The realization of the icosahedral Mackay packing[4] in B_6O and its macroscopic manifestation as icosahedral MTPs results from a combination of circumstances; these include the stability of the super-icosahedral unit that can serve as a nucleus and the appropriate rhombohedral distortion from ideal c.c.p. allowing unstrained icosahedral twinning. This distortion is closely related to the oxygen content, which is maximized in our high-pressure experiments[20].

It is remarkable that the bonding between the B_{12} units is consistent with the Mackay packing, similar to that encountered in β-rhombohedral boron in the centre, and to that of α-rhombohedral boron within the twin individuals. The twin boundaries and stacking faults observed near the twin boundaries correspond locally to a hexagonally close-packed type of stacking of the B_{12} icosahedra, rather than the normal (distorted) c.c.p. of α-rhombohedral boron. Such planar defects are expected to be of low energy because they do not affect the bonding with the first-neighbouring B_{12} units.

The B_6O MTPs are surely among the largest of self-assembled regular icosahedral particles found so far: there are $\sim 10^{14}$ atoms in a 20-μm icosahedron compared with 10^7 for typical virus particles. An additional feature of interest is that boron suboxide is known to be extremely hard[29], with abrasion qualities similar to those of diamond[30]. The icosahedral morphology of the grains makes them potentially useful for high-wear-resistance applications. Despite the uniaxial (trigonal) unit cell symmetry, all external faces of the MTPs have the same crystallographic orientation ($\{111\}_r$), and hence surface energy, which is presumably at a minimum. The faces should therefore wear at the same rate. The external icosahedral form, preferred under these high-pressure synthesis conditions, can be seen as a special state of condensed matter with long-range order that is neither three-dimensionally periodic nor quasicrystalline, but nevertheless possessing a higher degree of organization (and higher symmetry) than the individual crystals constituting the MTPs. □

Received 21 July; accepted 27 October 1997.

1. Thompson, D. A. W. *On Growth and Form* (Cambridge Univ. Press, 1961).
2. Madeley, C. R. & Field, A. M. *Virus Morphology* 2nd edn (Churchill Livingston, Edinburgh, 1988).
3. Kroto, H. W., Heath, J. R., O'Brien, S. C., Curl, R. F. & Smalley, R. E. C_{60}: Buckminsterfullerene. *Nature* **318,** 162–163 (1985).
4. Mackay, A. L. A dense non-crystallographic packing of equal spheres. *Acta Crystallogr.* **15,** 916–918 (1962).
5. Wales, D. J. Structure, dynamics, and thermodynamics of clusters: tales from topographic potential surfaces. *Science* **271,** 925–929 (1996).
6. Devouard, B. & Baronnet, A. Axial diffraction of curved lattices: geometrical and numerical modeling. Application to chrysotile. *Eur. J. Mineral.* **7,** 835–846 (1995).
7. Baronnet, A., Mellini, M. & Devouard, B. Sectors in polygonal serpentine. A model based on dislocations. *Phys. Chem. Mineral.* **21,** 330–343 (1994).
8. Evans, H. T. The crystal structures of cavansite and pentagonite. *Am. Miner.* **58,** 412–424 (1973).
9. Narayan, J., Srivatsa, A. R., Peters, M., Yokota, S. & Ravi, K. V. On epitaxial growth of diamond films on (100) silicon substrates. *Appl. Phys. Lett.* **53,** 1823–1825 (1988).
10. Williams, B. E., Kong, H. S. & Glass, J. T. Electron microscopy of vapor phase deposited diamond. *J. Mater. Research.* **5,** 801–806 (1990).
11. Doraiswamy, N. & Marks, L. D. Preferred structures in small particles. *Phil. Mag. B* **71,** 291–310 (1995).
12. Gammons, C. H. Hydrothermal synthesis of gold grains with apparent five-fold symmetry. *Can. Mineral.* **34,** 1–8 (1996).
13. Uyeda, R. in *Morphology of Crystals* (ed. Sunagawa, I.) (Reidel, Dordrecht, 1987).
14. Bachmann, P. K. & Wiechert, D. U. in *Diamond and Diamond-like Films and Coatings* 677–713 (NATO ASI Ser. B266, Plenum, New York, 1991).
15. Ohashi, W. & Spaepen, F. Stable Ga–Mg–Zn quasiperiodic crystals with pentagonal dodecahedral solidification morphology. *Nature* **330,** 555–556 (1987).
16. Dubost, B., Lang, J. M., Tanaka, M., Sainfort, P. & Audier, M. Large AlCuLi single quasicrystals with triacontahedral solidification morphology. *Nature* **324,** 48–50 (1986).
17. O'Keeffe, M. & Hyde, B. G. *Crystal Structures I: Patterns and Symmetry* (Mineralogical Soc. of America, Washington DC, 1996).
18. Lundström, T. in *Boron-Rich Solids* (eds Emin, D., Aselage, T., Beckel, C. L., Howard, I. A. & Wood, C.) 186–192 (AIP Conf. Proc. 231, Am. Inst. Phys., New York, 1991).
19. Vast, N. *et al.* Lattice Dynamics of Icosahedral α-Broon under Pressure. *Phys. Rev. Lett.* **78,** 693–696 (1997).
20. Hubert, H. *et al.* High-pressure, high-temperature synthesis and characterization of boron suboxide (B_6O). *Chem. Mater.* (submitted).
21. Hubert, H., Garvie, L. A. J., Buseck, P. R., Petuskey, W. T. & McMillian, P. F. High-pressure, high-temperature syntheses in the B–C–N–O system. Part I. Synthesis and characterization. *J. Solid State Chem.* (in the press).
22. Lundström, T. & Bolmgren, H. in *Proc. 11th Int. Symp. Boron, Borides and Related Compounds* (eds Uno, R. & Higashi, I.) **10,** 1–4 (JJAP Series, Tsukuba, 1994).
23. Kobayashi, M., Higashi, I., Brodhag, C. & Thévenot, F. Structure of B_6O boron-suboxide by Rietveld refinement. *J. Mater. Sci.* **28,** 2129–2134 (1993).
24. Lundström, T. & Andreev, Y. G. Superhard boron-rich borides and studies of the B–C–N system. *Mat. Sci. Eng.* A**209,** 16–22 (1996).
25. Bolmgren, H., Lundström, T. & Okada, S. in *Boron-Rich Solids* (eds Emin, D., Aselage, T., Beckel, C. L., Howard, I. A. & Wood, C.) 197–200 (AIP Conf. Proc. 231, Am. Inst. Phys., New York, 1991).
26. Donohue, J. *The Structures of the Elements* (Wiley, New York, 1974).
27. Naslain, R. in *Boron and Refractory Borides* (ed. Matkovitch, V. I.) 139–202 (Springer, Berlin, Heidelberg, 1977).
28. Hoard, J. L., Sullenger, D. B., Kennard, C. H. L. & Hughes, R. E. The structure analysis of beta-rhombohedral boron. *J. Solid State Chem.* **1,** 268–277 (1970).
29. Rizzo, H. F., Simmons, W. C. & Bielstein, H. O. The existence and formation of the solid B_6O. *J. Electrochem. Soc.* **109,** 1079 (1962).
30. Ellison Hayashi, C., Emond, G. T. & Kuo, S. Y. *Abrasion of surfaces with boron suboxide.* US Patent No. 920357 (1994).
31. Bagley, B. G. Five-fold pseudosymmetry. *Nature* **225,** 1040–1041 (1970).
32. Lee, S., Kim, S. W., Bylander, D. M. & Kleinman, L. Crystal structure, formation enthalpy, and energy bands of B_6O. *Phys. Rev. B* **44,** 3550–3554 (1991).

Acknowledgements. We thank K. Leinenweber for helpful discussions. This work was supported by the US National Science Foundation.

Correspondence should be addressed to H.H. (e-mail: hubert@asu.edu).

The timing of Pleistocene glaciations from a simple multiple-state climate model

Didier Paillard

Laboratoire de Modélisation du Climat et de l'Environnement, CEA/DSM, Centre d'Etudes de Saclay, 91191 Gif-sur-Yvette, France

The Earth's climate over the past million years has been characterized by a succession of cold and warm periods, known as glacial–interglacial cycles, with periodicities corresponding to those of the Earth's main orbital parameters; precession (23 kyr), obliquity (41 kyr) and eccentricity (100 kyr). The astronomical theory of climate, in which the orbital variations are taken to drive the climate changes, has been very successful in explaining many features of the palaeoclimate records[1]. Nevertheless, the timing of the main glacial and interglacial periods remains puzzling in many respects[2–5]. In particular, the main glacial–interglacial switches occur approximately every 100 kyr,

but the changes in insolation forcing are very small in this frequency band. Similarly, an especially warm interglacial episode, about 400,000 years ago[7], occurred at a time when insolation variations were minimal. Here I propose that multiple equilibria in the climate system can provide a resolution of these problems within the framework of astronomical theory. I present two simple models that successfully simulate each glacial–interglacial cycle over the late Pleistocene epoch at the correct time and with approximately the correct amplitude. Moreover, in a simulation over the past 2 million years, the onset of the observed prominent ~100-kyr cycles around 0.8 to 1 million years ago is correctly reproduced.

Although the 23-kyr and 41-kyr periodicities found in the palaeoclimate records seem to be almost linearly related to the insolation forcing[2], the largest climate variations of the past million years occur approximately every 100 kyr though the corresponding eccentricity changes are far too small to force the changes. Many hypotheses have been formulated to explain this '100 kyr problem', sometimes even involving other astronomical parameters[3]. Most of the suggested mechanisms are based on a nonlinear response of the ice-sheet dynamics to the forcing[4] or internal oscillations of the climate system[5,6]. Although some of these models compare well with the geological record in the spectral domain, all of them fail to reproduce the correct amplitude and phase of each glacial–interglacial cycle. In particular, one of the most prominent interglacial events, isotope stage 11, occurs at a time when the insolation variations are the smallest (around 400 kyr before present, BP) and therefore poses a strong challenge[4,7].

A multiple-state representation of the climate system may help solve these problems. The 100-kyr climate signal is not linearly related to the forcing[8], and thresholds between different states provide the simplest possible nonlinear mechanism. Furthermore, multiple states are known to exist in the climate system: in particular, there is increasing evidence that the ocean is such a system. The threshold model presented here is actually derived from a multiple-state ocean box-model[9].

The glacial–interglacial cycles are closely associated with the build-up and melting of the Laurentide and the Fennoscandian ice sheets at high northern latitudes. It is generally assumed, as a crude approximation, that summer insolation at high northern latitudes controls the ice-sheet volume, and hence the global climate. This is supported by the strong correlation[2,8] between global palaeoclimate records and the summer insolation at high northern latitudes. Therefore, this parameter is used in simplified models as the main external forcing. In the following, the term 'insolation' will refer to the daily insolation at 65° N at the summer solstice as computed by Berger[10].

I present two simple models that reproduce reasonably well the succession of glacial–interglacial cycles over the late Pleistocene. Whereas the power spectrum of the geological record is dominated by the 100-kyr periodicity over about the past 1 Myr, the 41-kyr periodicity seems to be dominant before[11]. I will therefore concentrate on the latest part of the record. The first model has three distinct states called **i** (interglacial), **g** (mild glacial) and **G** (full glacial). The second model is an extension of the first one.

Stommel[12] was the first to show that the oceanic thermohaline circulation could have multiple steady states. This was further verified in more sophisticated models[13–16]. The idea of a three-state structure came directly from the study of a simplified ocean model[9] whose dynamical structure is used here as our basic assumption.

If it is assumed that, depending on the insolation forcing and the ice volume, the climate system can enter three different regimes, and that the transitions occur according to Fig. 1, then a very simple model with few tunable parameters is obtained. This model undergoes an **i**–**g** transition as soon as the insolation falls below i_0. A **g**–**G** transition happens when the ice volume exceeds a threshold v_{max}, and finally a transition **G**–**i** occurs when the insolation increases above i_1. These transitions are assumed to be one-way: a **g**–**i** transition is impossible because the required insolation threshold is assumed to be beyond reach. The **g** regime is located between the **i** and **G** ones when, and only when, the ice volume is low: it should be low at the end of the **i** regime, and high after the **G** regime. Therefore, the **G**–**g** and **i**–**G** transitions are forbidden.

Without any explicit ice volume in this first model, I assume that the ice sheet needs some minimal time t_g in order to grow and exceed the volume v_{max} (**g** regime duration larger than t_g) and that the insolation maxima preceding the **g**–**G** transition must remain below the level i_3. The **g**–**G** transition then can occur at the next insolation decrease, when it falls below i_2.

Starting this conceptual model at the end of isotope stage 22 in a **G** regime, in an insolation minimum (at 875 kyr), we obtain the succession of states shown in Fig. 2. All the nine succeeding climate **G**–**i** transitions correspond to the main isotope transitions seen in the geological record. In particular, isotope stage 11.3 is correctly predicted at ~400 kyr BP. This model furthermore explains why stage 7.5 is warmer than the succeeding stage 7.3, although both insolation and ice volume would tend to suggest the opposite[1,17]: only stage 7.5 is a 'true' interglacial, while 7.3 corresponds to a particularly 'mild' glacial. The anomalous duration[1,7] of stage 11.3 is similarly explained by the particular shape of the forcing at this time.

This model is not very sensitive to parameter changes. Different threshold values will slightly offset the transitions by a few hundred years, but the overall shape will remain the same for a broad range of values. There is no significant changes when i_0 is between –0.97 and –0.64, i_1 between –0.23 and 0.32, i_2 between –0.30 and 0.13, i_3 between 0.97 and 1.16, and t_g between 27 kyr and 60 kyr. Even when the parameters are out of these bounds, the changes are minor: when i_0 is between –0.63 and –0.09, the succession of regimes remains the same except for present time, which becomes a **g** regime. When i_1 is chosen between 0.33 and 0.87, only the duration of stage 11.3 changes to become more comparable to other interglacial stages. The model is not very sensitive to the initial state: starting at 875 kyr BP in the wrong regime (**g** or **i**), the next two transitions are eventually misplaced, but the model rapidly recovers and results are unchanged afterwards (between 700 kyr and present).

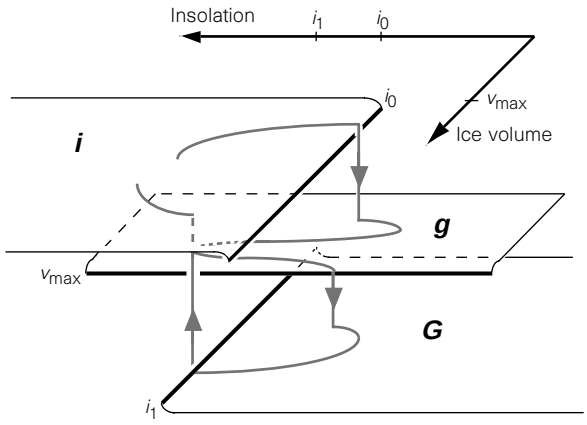

Figure 1 Schematic structure of the multiple-state system used. The climate is assumed to have three distinct regimes; **i**, **g** and **G**. The **i**–**G** transition is triggered when the insolation falls below the threshold i_0, the **g**–**G** transition occurs when the ice volume exceeds v_{max} and the **G**–**i** transition occurs when the insolation increases above the level i_1. Without any explicit ice volume in the first model, the v_{max} threshold is replaced by a minimal duration t_g for the **g** regime and the requirement that the previous insolation maximum is below a level i_3: the **g**–**G** transition occurs then at the next insolation decrease (below i_2). In the second model, the ice volume is explicitly represented.

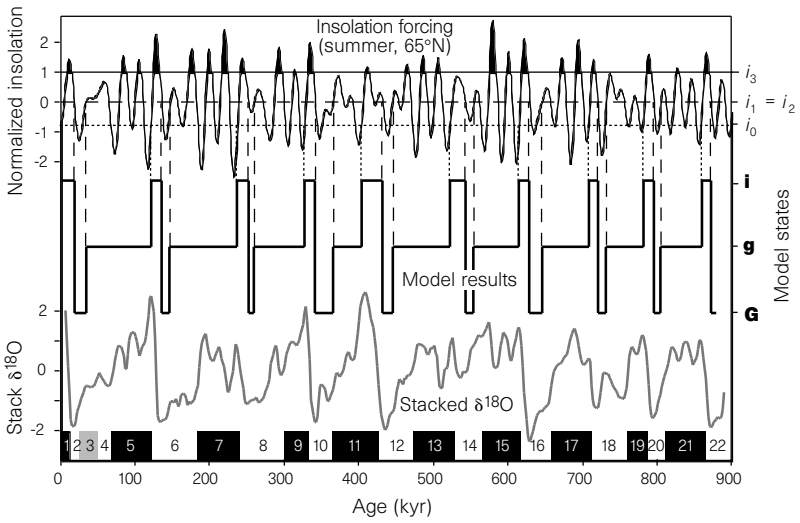

Figure 2 Results from the first idealized model (middle curve). The transitions (dashed vertical lines) are triggered by threshold (dashed horizontal lines) crossings of the insolation (upper curve, normalized to zero mean and unit variance). Insolation maxima above i_3 are in black: full glacial regimes **G** are associated with maxima below i_3. A stack of several geological oxygen isotope records[24] is plotted below for comparison, as well as the conventional isotope stage numbers. The threshold values are, in variance units, $i_0 = -0.75$, $i_1 = i_2 = 0$, $i_3 = 1$. The minimal duration of a **g** regime is $t_g = 33$ kyr.

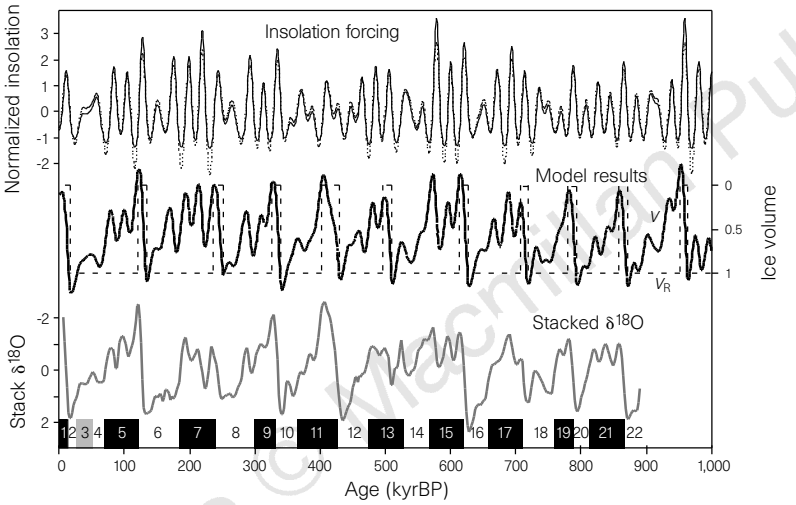

Figure 3 Results from the second model (thick middle curve). The value v_R is also plotted (dashed middle curve) in order to differentiate between **i** regimes ($v_R = 0$) and **g** or **G** regimes ($v_R = 1$). The model enters a **G** regime when the ice volume exceeds the value $v_{max} = 1$. The forcing F used here (continuous line) is a 'smoothed truncation' of the insolation used before (dashed line). An oxygen isotope stack record[24] is plotted below for comparison. The thresholds are, in variance units, $i_0 = -0.75$, $i_1 = 0$. The time constants are $\tau_i = 10$ kyr, $\tau_G = \tau_g = 50$ kyr and $\tau_F = 25$ kyr.

The same results can be obtained using another insolation curve (north of 35° N, from mid-April to mid-August, or with the Laskar[18] insolation curves) with only minor adjustments in the parameters.

These results highlight the fact that the interglacial stages defined in the isotope records are not directly associated with the largest maxima in the insolation curve. On the contrary, they systematically occur after the small ones[19]. Indeed, these small maxima eventually trigger a full glacial stage, then followed by an interglacial.

To go one step further, I constructed a differential version of the previous model. This second model still has the three regimes **i**, **g** and **G**, but the ice volume is allowed to change continuously. The criteria for the **i**–**g** and the **G**–**i** transitions are the same as before with the same threshold values. The **g**–**G** transition now occurs when the ice volume exceeds the value v_{max}, without any condition on the insolation. The model is, except for the thresholds, a simple linear one:

$$\frac{dv}{dt} = (v_R - v)/\tau_R - F/\tau_F$$

where v is the ice volume, R is the current climate regime (R = **i**, **g**, **G**), v_R are the reference ice volumes for the different regimes, F is the forcing, τ_R and τ_F are time constants. The ice volume is normalized to unity: $v_g = v_G = v_{max} = 1$, $v_i = 0$.

The forcing used here is a 'smoothed truncation' of the insolation in the previous model: F is computed using a truncation function f on the insolation, then normalizing to unit variance and zero mean, with:

$$f(x) = \frac{1}{2}\left(x + \sqrt{4a^2 + x^2}\right)$$

This results in a 'full' truncation: $f(x) = (x + |x|)/2$, when $a = 0$, and no truncation at all (after normalization), when $a = \infty$. We choose $a = 1$. This empirical adjustment accounts for the lower sensitivity of the ice volume during colder periods.

Starting at 1 Myr BP in a **g** regime with an ice volume $v_0 = 0.75$, we obtain results (Fig. 3) in good agreement with the isotope data. In this new experiment, the **i** regime of stage 13 occurs at a different time. Without reliable global estimates of the temperature during this time periods, it is difficult to prefer one or the other solution. No attempt was made to 'tune' the model to obtain a 'best possible' agreement with the data.

This second model is also quite robust. It is particularly insensitive to changes in τ_i and τ_G: any value of τ_G (0 to infinity) is acceptable and τ_i can be chosen between 0 and 15 kyr. The results will be almost unchanged with τ_g between 47 and 57 kyr, and τ_F between 23 and 29 kyr. The truncation parameter a can be chosen between 0.54 and 1.66. This second model also behaves quite correctly outside the limits given here, except for one or two transitions which will then be misplaced. Quite unexpectedly, stage 11 is one of the most robust features of this model. The most sensitive ones are stage 21, 19 and 3, where the ice volume

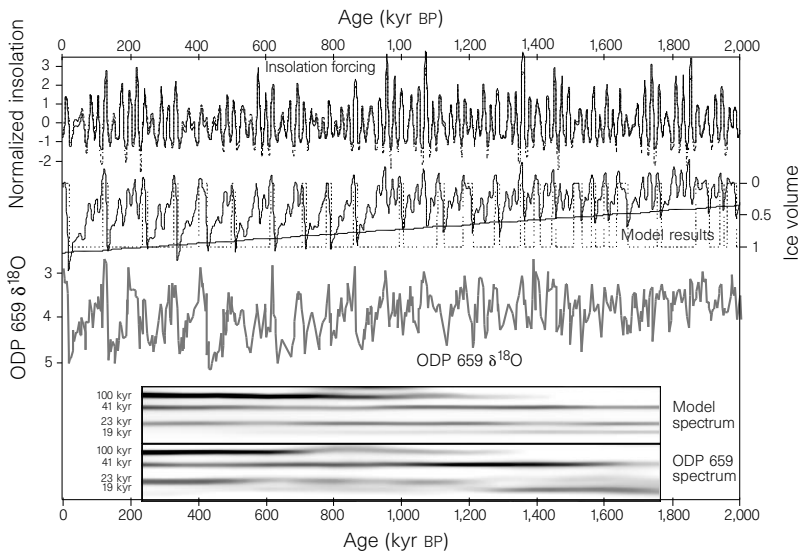

Figure 4 Same as Fig. 3 but with a time-varying threshold v_{max}. The insolation thresholds i_0 and i_1 are the same as before. The time constants are now $\tau_I = 5$ kyr, $\tau_G = \tau_g = 80$ kyr and $\tau_F = 28$ kyr. The ice volume threshold v_{max} (oblique thin line) increases linearly from 0.35 to 1.1 and a slight linear trend (3 W m^{-2} Myr^{-1}) is added to the insolation forcing (Laskar solution[18]) before truncation. The oxygen isotope record[25] from ODP site 659 is used for comparison. An evolutive spectral analysis of the two series is performed using the maximum entropy method and a sliding time window of 500 kyr. In both spectra, the 100-kyr periodicity appears around 1 Myr BP. Many aspects of the two series are quite similar, both in the time and frequency domains.

almost crosses the threshold v_{max} 'before time' (Fig. 3) and stage 7, where the ice volume barely crosses this threshold. For example, with no truncation on the forcing ($a = \infty$), all transitions remain unchanged except stage 7.3 and stage 3 which become interglacials. Starting in the wrong regime has also an effect limited to the next two cycles, after which the model recovers and results are unchanged. Using different high-latitude summer insolation curves does not affect the results, though the Laskar[18] ones appear preferable. I therefore believe the results from both models to be fairly robust.

In a last experiment covering 2 million years (Fig. 4), the model simulates correctly the onset of 100-kyr glaciations around 0.8–1 Myr BP. Over this time span, the slow tectonic activity induces slight ocean topographic changes and a possible decrease of atmospheric CO_2 concentrations[19]. Both will affect the threshold values of our conceptual model. The CO_2 decrease will also directly influence the radiative forcing. The results shown in Fig. 4 are obtained with a linearly increasing v_{max} threshold value, and a small linear trend added to the radiative forcing. The youngest part of the resulting simulation remains the same as before, and many aspects of the older part also compare reasonably well with the geological record, both in the time and spectral domains. It is nevertheless quite obvious that a more sophisticated model is needed to account for the detailed variability of the climate system over such a period of time.

Multiple states seem to be omnipresent, at least in climate models, and probably in the climate itself. The interpretation of palaeoclimate records of the past million years, in terms of a multiple-state system, seems therefore quite natural. The three-state model presented here seems to be a good candidate to explain some puzzling features of the Quaternary records, in particular the '100 kyr problem' as well as the 'stage 11 problem'. Furthermore, it is quite robust to changes in its parameters. It is not clear which physical components of the climate system may be responsible for such a trimodality, though the ocean is probably the best guess: coupled GCM experiments have shown that the Atlantic thermohaline circulation can be switched on or off with changing freshwater input[20] or changing atmospheric CO_2 concentration[21]. Some results on the last glacial inception[8,22,26] tend also to indicate that ocean circulation changes at high latitude precede the ice-sheet build-up. More generally, high-resolution palaeoclimate records show that abrupt transitions[23,26] are more the rule than the exception, thus suggesting the existence of thresholds. In any case, and in contrast to recent claims[3], this conceptual model clearly demonstrates that the geological record can easily be explained in the framework of the classical astronomical theory. If multiple states are an important characteristic of the climate system, much effort remains to be made in order to determine the critical thresholds of future climate changes. □

Received 17 January; accepted 4 November 1997.

1. Hays, J. D., Imbrie, J. & Shackleton, N. J. Variations in the earth's orbit: Pacemakers of the ice ages. *Science* **194,** 1121–1132 (1976).
2. Imbrie, J. *et al.* On the structure and origin of major glaciation cycles: 1. Linear responses to Milankovitch Forcing. *Paleoceanography* **7,** 701–738 (1992).
3. Muller, R. A. & MacDonald, G. J. Glacial cycles and orbital inclination. *Nature* **377,** 107–108 (1995).
4. Imbrie, J. & Imbrie, J. Z. Modelling the climatic response to orbital variations. *Science* **207,** 943–953 (1980).
5. Ghil, M. & Le Treut, H. A climate model with cryodynamics and geodynamics. *J. Geophys. Res.* **86,** 5262–5270 (1981).
6. Saltzman, B., Hansen, A. R. & Maasch, K. A. The late Quaternary glaciations as the response of a three-component feedback system to Earth-orbital forcing. *J. Atmos. Sci.* **41,** 3380–3389 (1984).
7. Howard, W. R. A warm future in the past. *Nature* **388,** 418–419 (1997).
8. Imbrie, J. *et al.* On the structure and origin of major glaciation cycles: 2. The 100,000-year cycle. *Paleoceanography* **8,** 699–735 (1993).
9. Paillard, D. Modèles simplifiés pour l'étude de la variabilité de la circulation thermohaline au cours des cycles glaciaire-interglaciaire. Thesis, Univ. Paris-Sud (1995).
10. Berger, A. Long-term variations of daily insolation and Quaternary climatic change. *J. Atmos. Sci.* **35,** 2362–2367 (1978).
11. Ruddiman, W. F., Raymo, M. E., Martinson, D. G., Clement, B. M. & Backman, J. Pleistocene evolution: northern hemisphere ice sheets and north atlantic ocean. *Paleoceanography* **4,** 353–412 (1989).
12. Stommel, H. M. Thermohaline convection with two stable regimes of flow. *Tellus* **13,** 224–230 (1961).
13. Bryan, F. High-latitude salinity effects and interhemispheric thermohaline circulations. *Nature* **323,** 301–304 (1986).
14. Manabe, S. & Stouffer, R. J. Two stable equilibria of a coupled ocean-atmosphere model. *J. Clim.* **1,** 841–866 (1988).
15. Rooth, C. Hydrology and ocean circulation. *Prog. Oceanogr.* **11,** 131–149 (1982).
16. Thual, O. & McWilliams, J. C. The catastrophic structure of thermohaline convection in a two-dimensional fluid model and a comparison with low-order box model. *Geophys. Astrophys. Fluid Dyn.* **64,** 67–95 (1992).
17. Jouzel, J. *et al.* Climatic interpretation of the recently extended Vostok ice records. *Clim. Dyn.* **12,** 513–521 (1996).
18. Laskar, J. The chaotic motion of the solar system: A numerical estimate of the chaotic zones. *Icarus* **88,** 266–291 (1990).
19. Raymo, M. The timing of major climate terminations. *Paleoceanography* **12,** 577–585 (1997).
20. Rahmstorf, S. Bifurcations of the Atlantic thermohaline circulation in response to changes in the hydrological cycle. *Nature* **378,** 145–149 (1995).
21. Manabe, S. & Stouffer, R. J. Century-scale effects of increased atmospheric CO_2 on the ocean-atmosphere system. *Nature* **364,** 215–218 (1993).
22. Cortijo, E. *et al.* Eemian cooling in the Norwegian Sea and North Atlantic ocean preceding continental ice-sheet growth. *Nature* **372,** 446–449 (1994).
23. Dansgaard, W. *et al.* The abrupt termination ofthe Younger Dryas climate event. *Nature* **339,** 532–534 (1989).
24. Bassinot, F. C. *et al.* The astronomical theory of climate and the age of the Brunhes-Matuyama magnetic reversal. *Earth Planet. Sci. Lett.* **126,** 91–108 (1994).
25. Tiedemann, R. *et al.* Astronomic timescale for the Pliocene Atlantic $\delta^{18}O$ and dust flux records of Ocean Drilling Program site 659. *Paleoceanography* **9,** 619–638 (1994).
26. Adkins, J. F. *et al.* Variability of the North Atlantic thermohaline circulation during the last interglacial period. *Nature* **390,** 154–156 (1997).

Acknowledgements. We thank S. Clemens and to M. Raymo for encouragement and comments on this Letter.

Correspondence and requests for materials should be addressed to the author (e-mail: paillar@aster-ix.saclay.cea.fr).